Contents list available at IJRED website

International Journal of Renewable Energy Development

Journal homepage: https://ijred.undip.ac.id

Research Article

Monitoring of Heat Flux Energy in the Northernmost Part of Sumatra Volcano Using Landsat 8 and Meteorological Data

Muhammad Yanis[a*], Nasrullah Zaini[a,b], Isra Novari[a], Faisal Abdullah[a,b], Bondan Galih Dewanto[c], Muhammad Isa[a,b], Marwan[a,b], Muzakir Zainal[a], Abdurrahman[d]

[a]*Geophysical Engineering Department, Universitas Syiah Kuala, Darussalam–Banda Aceh 23111, Indonesia*

[b]*Physics Department, Universitas Syiah Kuala, Darussalam-Banda Aceh 23111, Indonesia*

[c]*Geodetic Engineering Department, Universitas Gadjah Mada, Yogyakarta 55281, Indonesia*

[d]*Indonesian Agency for Meteorology, Climatology, and Geophysics, Aceh Besar, Indonesia*

Abstract. Geothermal energy, as a part of green and renewable energy, has been widely developed in the world to replace the current conventional fossil energy. Peut Sagoe is an active volcano in the northern part of Sumatra. The volcanic mountain has not been completely explored for geothermal and energy reserves study. This is due to the volcano locates in a high topography and surrounded by dense tropical forest, which makes it challenging to deploy geophysical instruments in the area. The Landsat 8 thermal infrared and meteorological data from 2013 – 2020 were used to estimate the energy resources by calculating the radiative heat flux (RHF) and measuring the energy lost annually through the heat discharge rate (HDR). We also used the normalized differential vegetation index (NDVI) for vegetation analysis, and estimation of its emissivity data. The mono-window algorithm was used to calculate the land surface temperature (LST). The Stefan–Boltzmann equation was utilized to analyze thermal infrared data for RHF, and ambient temperature and relative humidity data were acquired from the Indonesian Meteorological Agency (BMKG) database. The results showed that low vegetation values and high LST of 25°C–35°C were found in crater areas, which indicate the underground thermal activities of the mountain. It demonstrates that the maximum RHF values were 55 W/m^2 in 2013 and 37 W/m^2 in 2020. The HDR data were calculated by applying 15% of the RHF data, and the amounts of energy lost were 132.5 MWe and 64.5 MWe in 2013 and 2015 respectively. It increased to 186.4 MWe in 2017 and 89 MWe in 2020. Based on these predicted results, we conclude that the combination of thermal infrared imagery of Landsat 8 and meteorological data is an effective approach in estimating geothermal energy potential and energy loss of volcanoes situated in remote areas.

Keywords: Radiative heat flux, Peut Sagoe volcano, heat discharge rate, Landsat 8, geothermal.

Received: 20th June 2022; Revised: 16th August 2022; Accepted: 8th Sept 2022; Available online: 27th Sept 2022

1. Introduction

Indonesia lays at the confluence of three plates, Indo-Australia, Eurasia, and the Pacific, makes the region the third largest volcanic area in the world, reaching up to 30% (Bogie *et al.*, 2008; Suryadarma et al., 2010). This condition allows a large amount of geothermal energy to be stored in Indonesia, which is predicted to be 29 GW from 331 geothermal sites. At the same time, there are only 1698.5 MW or 9.3% from 11 locations with installed power plants (Kandari *et al.,* 2020). In the province of Aceh (northernmost of Sumatra), although there are many active volcanoes, none of these volcanoes have been developed into power plants. It is necessary to conduct several integrated studies as an effort to accelerate the development of geothermal powerplants, i.e., the Seulawah volcano with an estimated energy of 230 MWe (Marwan *et al.*, 2022). The water and temperature characteristics of the volcano have been assessed using geochemical method (Idroes *et al.*, 2019). Geothermal identities of the mountain were also studied by integrated geophysics methods, such as magneto telluric and transient electromagnetic (Ismail *et al.*, 2021; Marwan *et al.,* 2019b; Marwan *et al.*, 2021), remote sensing imagery of Landsat series for monitoring thermal activities from 2010 – 2020 (Zaini *et al.,* 2021), and the use of UAV sensors for high-resolution thermal monitoring (Marwan *et al.,* 2021).

Moreover, the other active volcanic mountain, the Jaboi volcano located at Weh island, has not been studied comprehensively with an estimation of 80 Mwe (Yanis *et al.*, 2022a). The geothermal manifestations, such as crater and hot spring have been developed into tourist site to accelerate the community's economy development (Borović and Marković, 2015; Marwan *et al.,* 2020). Besides the geothermal energy of Geuredong volcano in the center of Aceh (Yanis *et al.,* 2022b), and the Peut Sagoe volcano in the Pidie district have never been explored using geochemical and geophysical methods, so the

* Corresponding author
Email: yanis@unsyiah.ac.id (M.Yanis)

https://doi.org/10.14710/ijred.2023.47048
ISSN: 2252-4940/© 2023.The Author(s). Published by CBIORE

energy capacity of the volcano cannot be predicted (Yanis *et al.*, 2020b; Zaini *et al.*, 2022). This is because the volcanoes situate a high topography, so instrument mobility is very challenging. Figure 1 shows the topography of the Peut Sagoe volcano visualized from the Shuttle Radar Topography Mission (30 m for 1 pixel). The volcano has four peaks on the north-east side of the Peut Sagou and a crater 2.830 m above sea level, indicating volcanic activity in the subsurface. The common obstacles to volcanic exploration in Indonesia are generally the locations of the volcanoes in high terrain situations and the surrounding tropical forests compared to other regions (Bogie *et al.*, 2008; Mansoer and Idral, 2015).

Geophysics and geochemistry methods are successfully applied to geothermal areas, but the methods require significant financial support and are time-consuming (Chan *et al.*, 2018; Mohan et al., 2018). Various exploration methods need to be developed to increase geothermal energy utilization. Remote sensing is an emerging method that can be applied to examine volcanic activities. The remotely sensed data are available for long periods and can be accessed freely (Chan *et al.*, 2018; Yanis and Marwan, 2019), such as the geothermal potential analysis of the southwestern area of Saudi Arabia (Lashin and Al Arifi, 2014), Eastern Macedonia (Gemitzi *et al.,* 2021), and several geothermal fields in Italy (Silvestri et al., 2020a). In addition, the use of remote sensing data was not only for the analysis of volcanic potential, but it also allows for the calculation of the energy produced, as well as the estimation of the level of energy loss every year, which is helpful for economic analyses in the development of geothermal power plants (Mia *et al.,* 2013; Sekertekin and Arslan, 2019). This technique was also successfully applied to the Hatchobaru–Otake geothermal area in Japan (Mia *et al.,* 2019), Tuzla geothermal area in Turkey using ASTER data during the day and Landsat 8 data at night (Sekertekin and Arslan, 2019), and several volcanoes in Indonesia (Bogie *et al.,* 2008; Morifuji *et al.*, 2021).

Thermal infrared (TIR) sensors from the Landsat series are the primary data source in calculating various remote sensing parameters for geothermal studies (Darge *et al.,* 2019; Van der Meer *et al.,* 2014), such as ground surface temperature analysis, which is useful for detecting shallow thermal anomalies and which serves as an indicator of thermal information related to faults or volcanic complexes. In this study, we use a combination of Landsat 8 and meteorological data for the continuous monitoring of the thermal activities of the Peut Sagoe volcano, which can help determine the changes in thermal behavior in the hydrothermal system and the most active thermal areas for future development scenarios and in predicting future possible eruptive events (Mia *et al.,* 2013; Sekertekin and Arslan, 2019). In addition, Landsat series data can be used to compute the amount of energy produced through the radiative heat flux technique and the amount of energy lost through radiative heat loss (Chan *et al.*, 2018; Watson *et al.,* 2008).

2. Geological Setting of Peut Sagoe Volcano

The formation setting or rock distribution of geological structures on Sumatran Island, Indonesia is strongly influenced by tectonic activities from the Eurasia and Indo-Australia Plates (Bradley *et al.,* 2017; Sieh and Natawidjaja, 2000). In addition, on the mainland, there is a fault called the Great Sumatran Fault (GSF), which has a length of 1500 km from Lampung Indonesia to the Andaman Sea, India (Ghosal *et al.*, 2012; Natawidjaja and Triyoso, 2007; Yanis *et al.*, 2021a).

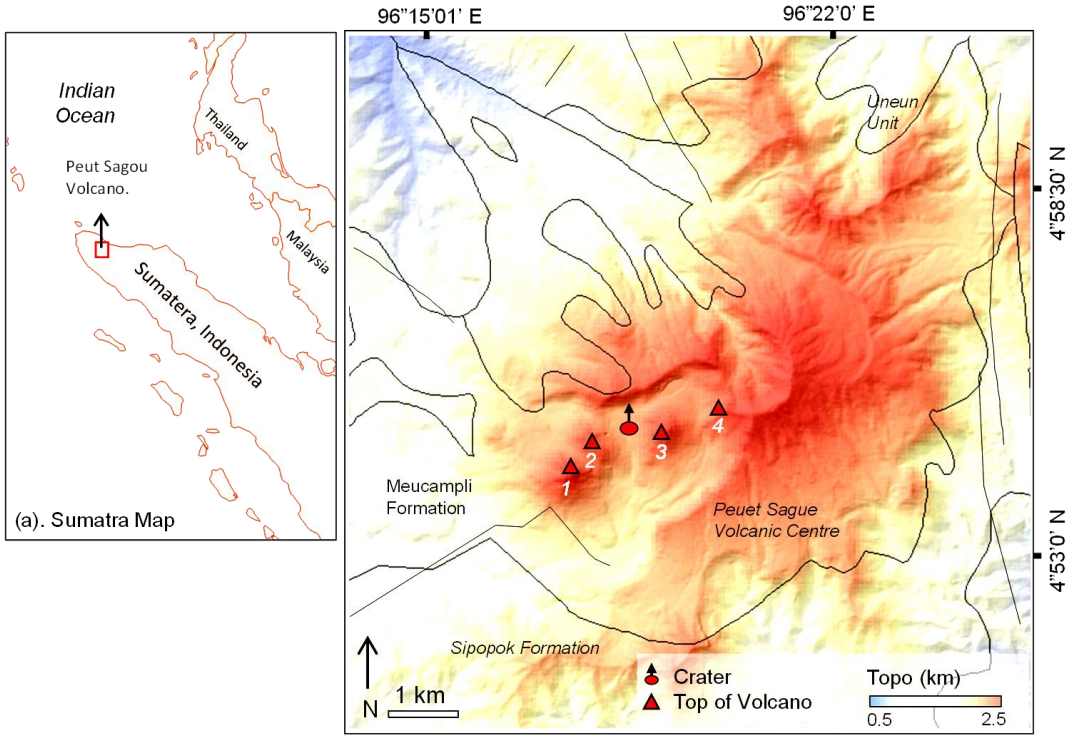

Fig. 1. The digital elevation model (DEM) showed the topography of the volcano at an altitude of 2.5 km. The black line is the boundary of rock formations based on geological data (Bennet *et al.,* 1996).

The Sumatran fault is divided into 20 segments, which has caused earthquakes of different magnitudes (Mosher *et al.*, 2008). However, in the northern part of Aceh the fault is divided into two parts: the Aceh segment extends to Aceh Island and has not shown significant earthquake activity (Muksin *et al.*, 2018; Yanis *et al.,* 2020a), and the Seulimum segment extends to Weh Island with a lot of earthquake activity and is a productive economic area (Rizal *et al.*, 2019; Yanis *et al.,* 2021b, 2020a). These two segments play a key role in the creation of various volcanoes in Aceh (Hochstein and Sudarman, 2008; Marwan *et al.,* 2019b), including the Peut Sagoe volcano (Zaini *et al.*, 2022).

Based on a geological map provided by (Bennet et al., 1996), the Peut Sagoe volcano is 15 km from the intersection of the two GSF segments in a northwest-southeast direction, with the Samalanga-Sipopok fault crossing from southwest–northeast on the northeast side of the mountain, which caused the 2016 Pidie Jaya earthquake which has significantly damaged infrastructure (Marwan *et al.,* 2019a). Morphologically, this volcano comprises numerous rocks, including Pleistocene andesite and basaltic, and Meucampli and Uneun formations in the form of quartzite and sandstone rocks dating from the Pleistocene to the Lower Miocene epochs, as seen in Fig.1. According to an unpublished document record from the Geological Agency, the Peut Sagoe volcano erupted multiple times, including in 1919, 1920, 1979, 1998, and most recently in 2000, when ash rain fell. However, because the volcano is in an area that is difficult to access, there are very limited local geological studies published

3. Data and Methodology

3.1 History of the Landsat Series

The USGS launched the Landsat civil satellite program in 1965, while the Landsat 1 was launched on July 23, 1972. After Landsat 5 stopped operating in November 2011, Landsat 6 failed to orbit (Aufaristama *et al.*, 2018). The Landsat satellites that still provide services are Landsat 7 and Landsat 8. The OLI and TIRS sensors are used by Landsat 8, and ETM^+ sensors are found on Landsat 7 (Chan *et al.*, 2018; Yanis *et al.,* 2020b). Landsat 7 is an eight-band satellite launched on April 15, 1999, using the ETM^+ sensor concept. This satellite was designed to operate for up to 5 years with a 16-day repeat acquisition. The main operational principle of Landsat 7 was to collect or acquire, archive, process, and distribute scientific data consistently (USGS, 2015). Since May 2003, a problem in the scan line correction on Landsat 7 has caused irreparable damage. However, it has been established that the radiometric and geometric sensors are unaffected (Williams *et al.,* 2006). After February 25, 2010, one of Landsat 7's eight bands is a single-band thermal band with a resolution of 30 m instead of 60 m (Qin *et al.*, 2011).

Using the TIRS sensor, the Landsat series has been used for geothermal energy applications for the past 50 years (Chan *et al.,* 2018). Many studies on geothermal exploration have demonstrated this application, including the use of Landsat 7 and Landsat 8 to identify or map potential geothermal areas by calculating the value of geothermal anomalies in the form of surface temperature (Mia *et al.*, 2014; Muñoz, 2014; Qin *et al.*, 2011), using a combination to map lineament zones in geothermal areas (Mwaniki *et al.*, 2015), and using different bands to map geothermal manifestations in a potentially geothermal aquifer (Yanis *et al.,* 2020b). Furthermore, with radiative heat flux (RHF) and radiative heat loss (RHL), Landsat 7 and Landsat 8 can be utilized to calculate the amount of energy lost from a geothermal area (Mia *et al.,* 2013; Sekertekin and Arslan, 2019). In this study, we used Landsat 8 thermal infrared data from 2013 to 2020 to estimate the amount of energy using the RHF technique and energy lost annually through the heat discharge rate (HDR).

3.2 Data Processing for the Landsat Series

Radiometric is the primary correction required for preparing satellite data. This correction is necessary to repair inaccuracies caused by the satellite's movement during orbit (Qin *et al.*, 2011), compensate for the blurring impact of the atmosphere, and convert digital number data to spectral light. However, there are no standards for preprocessing satellite image data, needing additional attention from satellite image data processors to provide more precise findings (Campbell, 2011). In addition, the normalized difference vegetation index (NDVI) is calculated as a parameter that provides an overview of the land cover/vegetation density of a region's surface of the Earth. Multichannel images generally reveal additional aspects of vegetation density or other density-related characteristics, such as biomass (Weng *et al.*, 2004). The NDVI value is generated by comparing the brightness of the red-light band with the brightness of the near-infrared light band as a greenish vegetation value. Mathematically, the NDVI is calculated using eq. (1).

$$\mathrm{NDVI} = \frac{(\mathrm{NIR}-\mathrm{RED})}{(\mathrm{NIR}+\mathrm{RED})}, \quad (1)$$

NDVI is the normalized difference vegetation index, and NIR and RED are bands 5 and 4, respectively. It is also possible to assess a region's fractional size by computing the value of a region's land cover vegetation fraction, which is also known as proportional vegetation (PV). Equation 2 shows that the vegetation fraction can be any value between 0 and 1.

$$\mathrm{PV} = \left(\frac{\mathrm{NDVI}-\mathrm{NDVI_s}}{\mathrm{NDVI_v}-\mathrm{NDVI_s}}\right)^2, \quad (2)$$

The NDVIs is the NDVI values in soil areas, NDVIv is the NDVI values in densely vegetated regions, and PV is the vegetation/land cover fraction. The emissivity value is calculated using the PV value obtained from eq. (2), which is defined as a surface's ability to transform heat energy into radiant energy. Emissivity is a crucial characteristic in determining the value of land surface temperature, computed mathematically using eq. (3).

$$\varepsilon = \mathrm{m} \times \mathrm{PV} + \mathrm{n}, \quad (3)$$

where m and n are variables determined separately on the emissivity of soil and vegetation with values of 0.004 and 0.986 (Weng *et al.*, 2004). Furthermore, the brightness temperature data, a measure of microwave radiation emission into the Earth's atmosphere, are calculated, collected, and analyzed. According to the below equation for calculating brightness temperature, variations in spectral emission can be expressed in Kelvin units, and therefore, the temperature value is computed using eq. (4).

$$\mathrm{BT} = \left(\frac{\mathrm{K_2}}{\left(\frac{\mathrm{K_1}}{\mathrm{L_\lambda}}+1\right)}\right) - 273, \quad (4)$$

The BT is a temperature sensor, K_1 and K_2 are the thermal conversions constant bands–x, and L_λ is the spectral radian band–x (watt/(m^2*srad*μm). In addition, the value of land surface temperature (LST) will be determined, which is the

temperature of an object's outermost section that is influenced by the object's physical qualities, such as emissivity, thermal conductivity, and specific heat capacity (Romaguera *et al.*, 2018). The radiation temperature coming from infrared radiation is referred to as LST, defined as the average surface temperature of a surface displayed in pixels calculated using eq. (5).

$$\mathrm{LST} = \frac{\mathrm{BT}}{1 + \left(\frac{\lambda \times \mathrm{BT}}{\mathrm{P}}\right) \ln(\varepsilon)}, \quad (5)$$

where LST denotes land surface temperature in Kelvin, PV is the percentage of vegetation, and λ denotes the wavelength in band 10, which is 11.5 m as the TIRS band's effective wavelength. The outcome of calculating $h \times \frac{c}{s}$, which is 14380 μmk, is P. The investigation of the LST anomalies is an important factor in determining whether a geothermal area has the potential to be developed. As a result, many LST studies have been conducted around the world, such as the one conducted by (Qin *et al.*, 2011) in Tengchong, China, using Landsat ETM$^+$.

3.3 Radiative Heat Flux (RHF)

Geothermal systems are defined by detecting geothermal anomalies determined by the presence of a high-temperature gradient. The RHF represents the radiant heat flux as an energy loss event in a geothermal area in three ways: radiation, conduction, and convection. The estimation of heat loss is usually conducted using geochemical methods (Ramírez-González et al., 2019). The parameter variables used in the RHF equation include the atmospheric transmissivity value obtained based on the results of the calculations using the NASA calculator on https://atmcorr.gsfc.nasa.gov/. The surface temperature value (LST) of the volcanic area, and the ambient temperature value obtained from Indonesian Agency for Meteorology (BMKG), which is shown in Table 1.

By subtracting the temperature of the geothermal area from the temperature of the area with the same topography, the RHF computation can be based on the Stefan–Boltzmann law, which is mathematically written as follows (Mia *et al.*, 2013).

$$\mathrm{Q_r} = \tau \sigma \varepsilon \left(\mathrm{T_s}^4 - \mathrm{T_a}^4\right), \quad (6)$$

where τ is atmospheric transmissivity, σ is the Stefan–Boltzmann constant (5.6704×10^{-8} $\mathrm{Wn^{-2}\ K^{-4}}$), ε is emissivity, Ts is the value of the land surface temperature, and Ta is the background temperature in the form of ambient temperature. The RHF value that has been obtained is then used to determine the amount of energy from a geothermal system that requires the value of energy loss, and the amount of energy lost in a geothermal area is calculated by adding the pixel values with positive RHF values and multiplying by the pixel area. For example, the pixel area for Landsat 8 (A = 30 × 30 m) can be computed using the equation below.

$$\mathrm{RHL} = \left(\sum \mathrm{RHF_+}\right) \times \mathrm{A}, \quad (7)$$

where $\mathrm{RHF_+}$ is the number of positive RHF values in the area used, and A is the pixel area used for Landsat data collection (Mia *et al.*, 2019). To estimate heat loss that is not affected by the sun's rays, it is necessary to calculate the total heat loss. The HDR calculation is performed using eq. (8).

$$\mathrm{HDR} = \left(\left(\sum \mathrm{RHF_{pixel+}}\right) \times \mathrm{A}\right) \times \mathrm{C}, \quad (8)$$

Table 1
Parameters in the calculation of RHF

Parameter	Year			
	2013	2015	2017	2020
Relative humidity (RH)	83.6	84.7	86.2	84.3
Atmospheric transmissivity	1	0.9	1	0.89
Ts (LST)	35.24	30.45	38.96	33.16
Ta (ambient temperature)	26.5	25.59	26.3	26.5

where HDR is the total heat energy loss without the influence of the sun (MW), $\mathrm{RHF_{pixel}}$ is the positive RHF pixel of a picture, A is the area of each pixel (m^2), and C is the coefficient between HDR and RHL (C = 6.49 or 15%).

4. Results and Discussion

4.1 Vegetation of the Volcano

The bands 5 (NIR) and 4 (RED) were utilized to calculate the NDVI value. According to the research area, these two bands undergo a data cutting step and data preprocessing, which is divided into two stages: the DN (Digital Number) to TOA reflectance calibration stage and the sun elevation calibration stage. The parameters utilized in the computations were derived from the Landsat data metafile for each year; the calibration results for both bands are depicted in Fig. 2, which shows a more accurate image. This is directly tied to the growth in the value of each pixel and the quality of the NDVI and LST values.

Before calculating the NDVI data, we first performed a topographical analysis using DEM, as shown in Fig. 1. This volcano has four peaks, three of which are aligned north-south at an altitude of 2780 m, and a peak on the northeast side is characterized by barren land as a sign of ancient eruptions. Signs of geothermal presence can also be seen from active craters in volcanic areas, so the area will be dominated by low vegetation. Shortwave infrared data combined with bands 7, 6, and 4 show the same thing. The entire volcanic area is dominated by high vegetation, but there is a significant vegetation contrast in the crater area, as shown in Fig. 3a. Furthermore, NDVI calculations were carried out using reflectance spectral data from the NIR and RED spectra to provide a fast estimate of the presence of vegetation (Marwan et al., 2021; Sekertekin and Arslan, 2019).

The NDVI calculations were conducted by utilizing band 5 and band 4, calibrated into the reflectance spectral data. The NDVI value varies from −1 to 1, and unvegetated land has a value of $-1 < \mathrm{NDVI} < -0.03$. Land having a negative NDVI value is designated as water land or wetlands (Weng et al., 2004), land with an NDVI value of $-0.03 < \mathrm{NDVI} < 0.15$ is classified as land with a very low level of vegetation, and land with a value of $0.15 < \mathrm{NDVI} < 0.25$ is classified as land with a low vegetation level, land with a value of $0.25 < \mathrm{NDVI} < 0.35$ is classified as land with a moderate level of vegetation, and land with a value of $0.35 < \mathrm{NDVI} < 1$ is classified as land with a high level of vegetation. Regarding (Mia et al., 2014) classified the range of NDVI values for healthy vegetation as a range of > 0.5, so we plot the value > 0.5 as a vegetated area. Briefly, we only present the NDVI values for the Peut Sagoe volcano in 2013 as shown in Fig. 3b. In 2013, the lowest NDVI value was –0.29, and the highest value was 0.85.

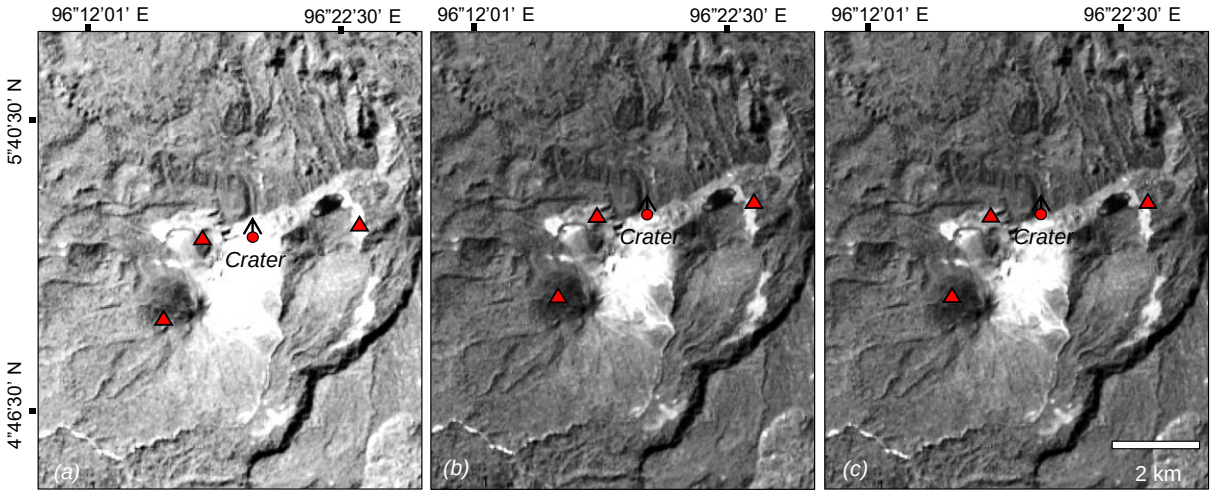

Fig. 2. (a) Landsat band 4 images before correction, (b) band 4 after atmospheric calibration of the reflection stage, and (c) band 4 after atmospheric calibration of sun elevation.

A dark green scale of 0.7 to 0.8, which dominates most of the Peut Sagoe volcanic area this year, indicates the level of high and healthy vegetation. Meanwhile, other volcano areas, such as the crater section of the vegetation level on the Peut Sagoe volcano, have low values with a red scale in the −0.2–0.2 range. A scale indicates the existence of unoccupied land, water, or wetlands within this range. The Kemiki crater and lake are seen in the research area. Furthermore, the presence of clouds in the image may be seen in the low vegetation level with a red scale in the southern part. The altered land is identified as mixed land, consisting of barren land and low vegetation, using a yellow color scale with 0.2–0.4. Then, there is a terrain with moderate to high vegetation levels with a color scale of 0.5 to 0.7 on a bright green scale. Moreover, the vegetation fraction or the vegetation canopy of a region is determined as the value of the proportion of vegetation (PV) that has a close link with NDVI, particularly as a derivative, where this PV parameter is required for calculating the NDVI value that accounts for the effects of changes in vegetation in the measurement region (Chan *et al*., 2018), as shown in Fig. 3c.

An area with PV = 0 indicates the presence of barren land, whereas an area with PV = 1 implies a canopy with high vegetation. As shown in Fig. 3d, the range of PV values in 2013 was 0 to 1. The crater region is denoted by a red scale with a PV value between 0 and 0.3, indicating that this area consists of barren land. In addition, the clouds in the image are denoted by this scale. Therefore, it is important to consider the existence of clouds when assessing the PV value in the image. To find objects that can be identified as having low PV values, such as Lake Kemiki, it is also necessary to refer to the geological and geomorphological conditions of the research area. Furthermore, the scale is orange, and a small portion is yellow, suggesting the presence of an alteration zone with PV values ranging from 0.3 to 0.6 and from 0.6 to 0.7, respectively. The color scales that dominate the Peut Sagoe volcano area characterized by moderate to high PV levels are bright green and dark green, with PV values of 0.7–0.8 and 0.8–1, respectively.

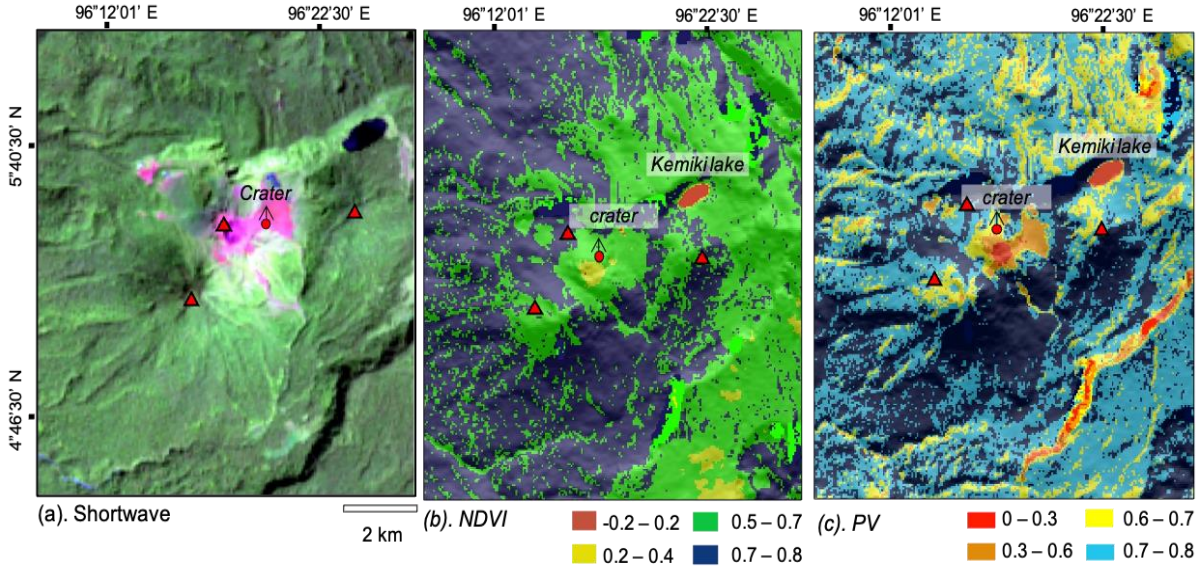

Fig. 3. (a) A shortwave infrared composite band from bands 7, 6, and 4 that can map the vegetation area, (b) the NDVI value for 2013 that shows the vegetation level, and (c) the propagation vegetation value required as a parameter for calculating temperature.

4.2 Temperature Analysis

In general, geothermal systems form because of heat transfer from nearby sources via conduction and convection. Reservoirs with high permeability can provide a site for fluid to concentrate below the surface, and this activity can be tracked through temperature changes above the surface. To compute the Peut Sagoe volcano's temperature, it is important to determine the ground surface's emissivity, a proportionate factor in detecting black body emission and predicting light emission. Furthermore, LSE aids in reducing errors while estimating LST values (Sekertekin and Arslan, 2019). To calculate the emissivity value, proportional vegetation data derived from the previous NDVI are utilized (Sobrino *et al.*, 2008). In addition, the LST value can be calculated using thermal infrared data, which offers speed and reliability in estimating the surface temperature's physical parameters and are faster and more cost-effective (Silvestri *et al.*, 2020b). In this study, one of the TIRS bands, band 10, was utilized to calculate the LST value.

The selection of band 10 as part of the TIRS band was because the TIRS band is typically used to calculate thermal anomalies, which are not solar reflections but rather solar radiation. LST as a geothermal anomaly is also one of the determinants of geothermal potential as geothermal on the surface is typically associated with heat sources below the surface and is the principal controller of the Earth's effective radiation temperature. According to (Qin *et al.*, 2011), the Earth's ground surface temperature is influenced by external variables such as solar radiation and the Earth's interior. The latter is the most important element in raising the temperature on a local scale. Solar radiation, landforms, and the presence of earthquakes are some of the more specific factors. Nevertheless, the LST data are influenced by physical qualities like emissivity. Because they are united in total emission, emissivity is an essential component of LST. As a result, the emissivity value becomes a critical element for determining the accuracy of LST readings in LST computations (Sekertekin and Arslan, 2019).

According to (Qin et al., 2011), this algorithm requires fewer parameters than other algorithms such as mono-window. These parameters represent the estimated LSE and brightness temperature parameters. Specifically, Fig. 4 depicts the emissivity and surface temperature data. The emissivity value obtained in 2013 ranged from 0.8 to 0.99, where the minimum value denotes barren land, no vegetation, or water area. This scale is shown in a light purple to indicate the existence of the Peut Sagoe volcano crater and waters in the form of Lake Kemiki. This scale characterizes cloud areas acquired by satellites in the computation of emissivity. At the same time, land with high and healthy vegetation levels is designated with a value of 0.99, which dominates the research area. Then, there is a land with moderate vegetation in the eastern section.

Data from the LST calculation in this study have been cleared by reclassifying the data value in the QA band and setting the cloud data value to zero. The surface temperature of Peut Sagoe was measured and found to range from 10.64°C to 35.24°C. The 2013 LST image represents territory with very low-temperature values ranging from 0°C to 16°C. This anomaly is found on top of the volcano and in other regions, such as hilltops in the east. Volcanoes with temperatures between 16°C and 18°C are located in the southern and eastern parts of the volcano. According to the NDVI data, this location has a high level of vegetation, which means that the radiation from the surface would be lower. Surface temperatures between 18°C and 25°C show that the land is at a moderate LST. Meanwhile, high temperatures of 25°C–35°C have been recorded in various areas around the crater and in the northern and western regions of the Peut Sagoe volcano, which are in direct contact with the volcano's thermal activity.

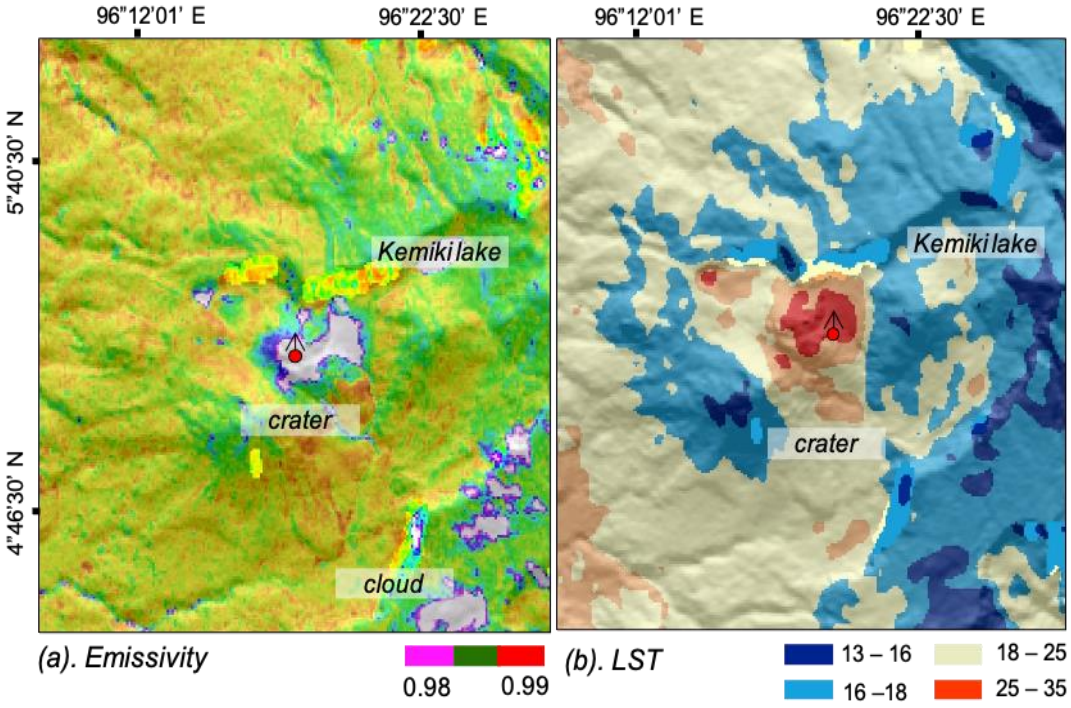

Fig. 4. (a) The emissivity value obtained from the Peut Sagoe volcano, and (b) the temperature distribution calculated from the Landsat 8 thermal data band.

4.3 Monitoring of Geothermal Energy

Radiative Heat Flux (RHF) is the value of the geothermal radiation emitted by the Earth, which can be in the form of heat or geothermal flux reflected by the Earth's surface and reradiated as the effect of solar radiation (Mia *et al.*, 2013). The RHF value is mainly used to measure energy loss in geothermal locations. The Stefan–Boltzmann equation is used to compute the RHF value, as was conducted by (Mia *et al.*, 2017). In the calculation of the RHF value in 2013, the ambient temperature was 26.5°C, and the atmospheric transmissivity was 1 τ. Thus, the energy estimate is obtained as shown in Fig. 5. It is known that orange represents land with a positive value for each pixel to a red scale with an RHF value ranging from 0 to 35 W/m^2. The area around the crater and a small area to the east of the Peut Sagoe volcano identified as altered land is occupied by land of this scale.

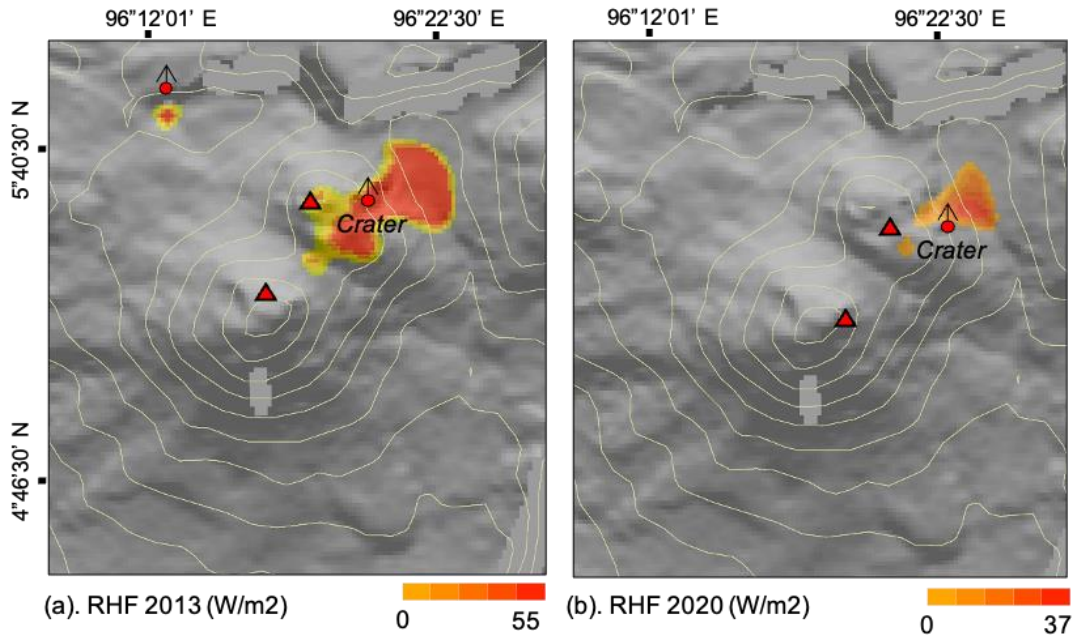

Fig. 5. Radiative heat flux values of the Peut Sagoe volcano in 2013 and 2020. The RHF is only calculated in the crater and warm ground area because it is not affected by vegetation.

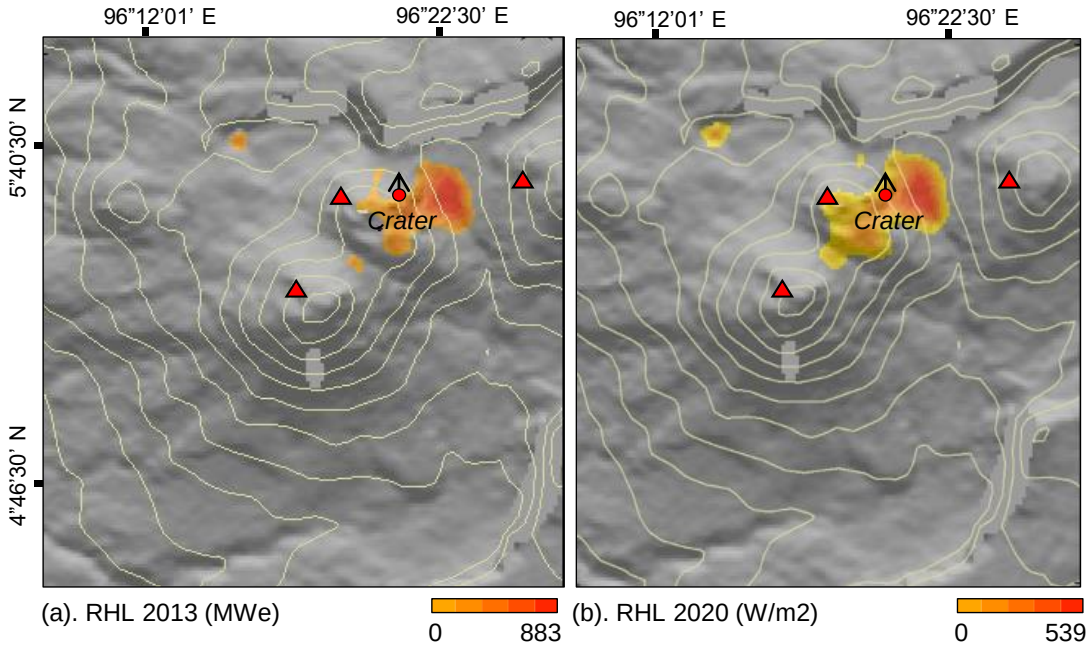

Fig.6. The radiative heat loss value of the Peut Sagoe volcano shows the amount of energy obtained in Mwe, (a) in 2013, and (b) in 2020.

The crater zone and small land in the eastern part of the Peut Sagoe volcano are then occupied by land with a red color scale and a high RHF value spanning from 35 to 54.96 W/m^2. The area with positive pixel values is in the range of very low NDVI values with high LST values if it is related to the NDVI level. Other areas in green to yellow correspond to land with a negative RHF value per pixel, moderate to high NDVI values, and low LST values. The RHF positive pixel value in 2020 is depicted by a red to orange gradation color scale with 0–36.93 W/m^2, representing the region of altered land around the Peut Sagoe volcano's crater (Fig. 5b). The top part of the crater is designated as orange because it has a positive pixel value.

In addition, no small land with a positive red color scale was identified in the eastern part of the year. In reality, between 2013 and 2017, this land was detected as having a positive RHF pixel value. This is conceivable because the vegetation level in this portion is higher than that in the crater area. Furthermore, because the LST value was lower in 2015 and 2020 than in 2013 and 2020, it was determined that the heat stored beneath the surface of the region could not be radiated because the level of vegetation influenced it. Moreover, the RHL value was chosen which is controlled by three heat transfer events: conductive, convective, and radiation heat losses (Mia *et al.,* 2017). As indicated in Fig. 6, the coverage area per pixel employed in this study was adjusted to the Landsat 8 coverage area per pixel, which was 30 × 30 m^2.

In 2013, a relatively high radiative heat loss (approximately 883.9 MWe) was obtained. The maximum radiative heat losses in 2015 and 2020 were calculated to be 430 and 593 MWe, respectively. The maximum LST value, ambient temperature, and RHF value determine the contrast between the maximum RHL values for each year in this study. According to the research findings, the geothermal area will lose more energy during low ambient temperatures, low LST temperatures, and high RHF values. Based on the radiative heat flux value, it is known that land with high volcanic activity, such as crater areas and manifestation land marked by alteration, experiences energy loss. The land that endures energy loss is shown using a color scale grading yellow to red. The red color scale shows a high degree of RHL located in the crater area, south of the Peut Sagoe volcano. Meanwhile, the altered ground around the crater and the western section identified in 2013 and 2017 show energy loss, and the high LST temperatures also influence the area undergoing energy loss.

The radiative heat loss calculation results show an extremely high energy estimation value ranging from 34 to 921 Mwe due to external factors such as the sun's effect. As illustrated in Fig. 7, the (HDR) is calculated to achieve improved radiative, conductive, and convective heat loss values in the manifestation area and geothermal sites in general. The relation coefficient between radiative heat flux and radiative heat loss is 15% when computing the HDR value (Mia *et al.,* 2013; Mia *et al.,* 2017). In 2013, the HDR value in regions suffering from energy loss events ranged from 0 to 132.5 MWe, with the crater area and a small portion to the west of the Peut Sagoe volcano exhibiting extremely high HDR values. In 2015, 2017, and 2020, the most significant values for the Peut Sagoe volcano crater were 64.5, 186.4, and 89 MWe, respectively. In addition to the intriguing crater region, the HDR calculation reveals the area in the western section of the Peut Sagoe Volcano. This region is reasonably far from the Peut Sagoe volcano's crater. However, in 2013 and 2020, a red color scale with high HDR values revealed its existence.

Overall, it can be seen in Fig.8 the change in heat flux energy of the Peut Sagoe volcano, where the highest RHF was in 2015 (77.2 MWe). The pattern of energy changes in 2013 - 2020 showed a low value in 2013, then increased in 2017, and returned to a low value in 2020, indicating a change in energy from subsurface magmatic activity. While the RHL data used to estimate energy loss shows a different pattern; namely in 2013 and 2017 the value of energy loss was very high, while the energy loss was low in 2015 and 2020, namely 430.4 and 59.3 Mwe, respectively. The same pattern is also shown by the HDR data used for energy estimation in volcanoes, so the same changes are obtained with the RHL value, where the highest energy was acquired in 2013 (132 MWe) and 2017 (186.5 MWe), so that in the following year due to energy loss then obtained a low HDR response as in 2015 and 2020.

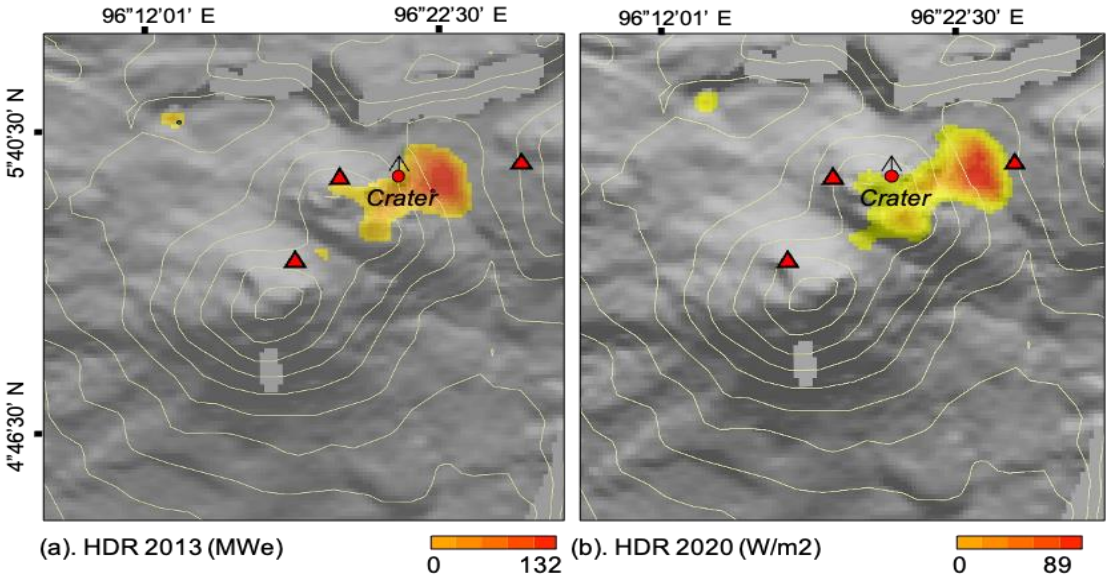

Fig. 7. Heat discharge rate value of the Peut Sagoe volcano shows the amount of energy obtained yearly in Mwe, namely, (a) 2013 and (b) 2020.

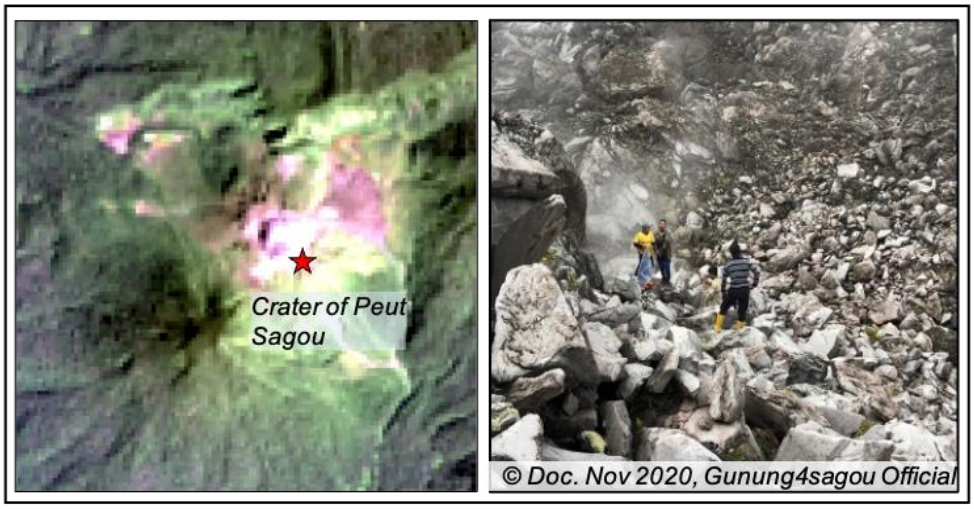

(a). Map and documentation of crater in Peut Sagou volcano

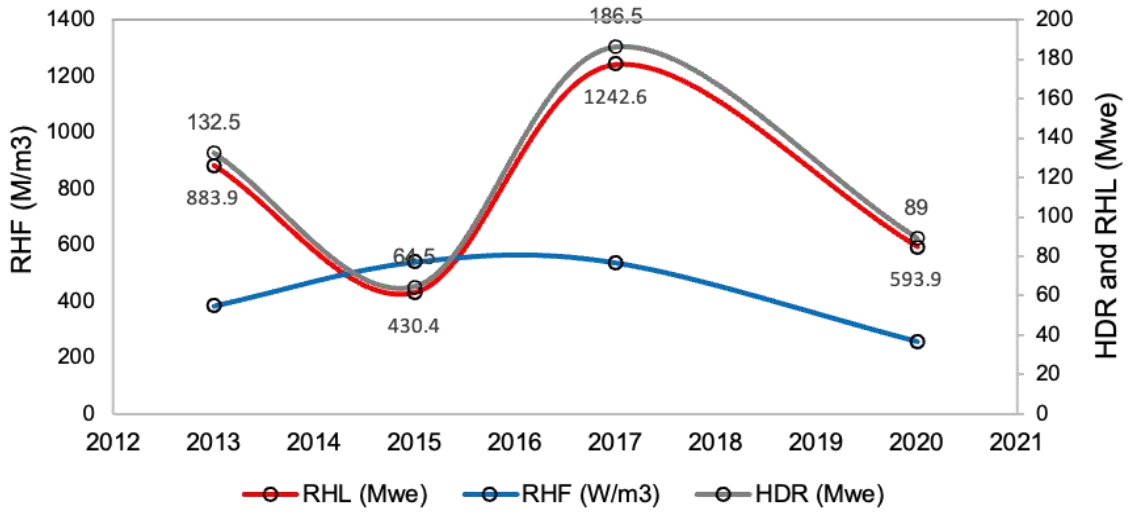

(b). The pattern of changes in the estimation and energy loss

Fig. 8. Estimated and predicted yearly energy loss (2013 – 2020) at the Peut Sagoe volcano using radiative heat flux, heat loss, and heat discharge rate techniques. (a) The map showing a location of the crater from Landsat 8 true color composite, as well as documentation in the crater area taken in November 2020, while (b) a pattern that obtained from the energy analysis of the volcano.

5. Conclusions

Generally, the results of the NDVI analysis showed the surrounding volcanic area is dominated by dense vegetation. In contrast, the locations related to the geothermal manifestations, such as craters, hot springs, and warm ground yielded low vegetation values that indicates volcanic activities of the mountain. Furthermore, as a response to the volcanic activities, shortwave infrared data showed a contrast of the crater area with its surrounding area. Surface temperature illustrated that high LST values were dominated at the crater area in the range of 25°C–35°C as compared to the surrounding area, which is between 16°C and 25°C. The results of calculations using radiative heat flux processed using thermal data and parameters from the Indonesian Agency for Meteorology, the energy estimation in the crater area was 55 W/m^2 in 2013 and 37 W/m^2 in 2020. The calculated energy loss for each year using the radiative heat loss technique showed a reasonably significant energy loss: 883.9 MWe in 2013 and 430 MWe and 593 MWe in 2015. However, the energy loss was due to an external factor (the effect of the sun), so the energy loss values obtained from the heat discharge rate were 132.5 MWe in 2013 and 64.5 MWe in 2015, which increased to 186.4 MWe in 2017 and 89 MWe in 2020. The Landsat 8 data analysis revealed a good correlation between NDVI and the surface temperature, as well as the estimated loss of energy with HDR that had been corrected for sun and surface temperature. It can be concluded that the thermal infrared data of Landsat 8 can be used to estimate the geothermal energy reserves and monitor heat loss from any fumarole area effectively.

Acknowledgments

We are thankful to Seulawah Institute Publishing as a research group that has supported for providing computer equipment for data processing.

Funding: This paper is part of the Penelitian Dasar Kompetitif Nasional (PDKN) grant by the Indonesian Ministry of Education, Culture, Research and Technology with No. 46/UN11.2.1/PT.01.03/DRPM/2022.

Conflicts of Interest: The authors declare that we have no conflict of interest in this paper.

Author Contributions: M,Y; N,Z; M,I: Conceptualization, methodology, formal analysis, writing—original draft, M,M.; M,Z; A,A supervision, resources, project administration, M,Y; M,Z; I,N.; writing—review and editing, project administration, validation, F,A;.; writing—review and editing, project administration, validation. All authors have read and agreed to the published version of the manuscript.

References

Aufaristama, M., Hoskuldsson, A., Jonsdottir, I., Ulfarsson, M., Thordarson, T., 2018. New Insights for Detecting and Deriving Thermal Properties of Lava Flow Using Infrared Satellite during 2014–2015 Effusive Eruption at Holuhraun, Iceland. *Remote Sens.* 10, 151. https://doi.org/10.3390/rs10010151

Bennet, M., Doyle, P., Larwood, J., Prosser, C., 1996. Geology on your Doorstep. Geol. Soc. Publ. 270pp.

Bogie, I., Kusumah, Y.I., Wisnandary, M.C., 2008. Overview of the Wayang Windu geothermal field, West Java, Indonesia. *Geothermics* 37, 347–365. https://doi.org/10.1016/J.GEOTHERMICS.2008.03.004

Borović, S., Marković, I., 2015. Utilization and tourism valorisation of geothermal waters in Croatia. Renew. *Sustain. Energy Rev.* 44, 52–63. https://doi.org/10.1016/J.RSER.2014.12.022

Bradley, K.E., Feng, L., Hill, E.M., Natawidjaja, D.H., Sieh, K., 2017. Implications of the diffuse deformation of the Indian Ocean lithosphere for slip partitioning of oblique plate convergence in Sumatra. *J. Geophys. Res. Solid Earth* 122, 572–591. https://doi.org/10.1002/2016JB013549

Campbell, J. and R.H.W., 2011. Introduction to Remote Sensing, Fifth Edit. ed. The Guilford Press, London.

Chan, H.P., Chang, C.P., Dao, P.D., 2018. Geothermal Anomaly Mapping Using Landsat ETM+ Data in Ilan Plain, Northeastern Taiwan. *Pure Appl. Geophys.* https://doi.org/10.1007/s00024-017-1690-z

Darge, Y.M., Hailu, B.T., Muluneh, A.A., Kidane, T., 2019. Detection of geothermal anomalies using Landsat 8 TIRS data in Tulu Moye geothermal prospect, Main Ethiopian Rift. *Int. J. Appl. Earth Obs. Geoinf.* https://doi.org/10.1016/j.jag.2018.08.027

Gemitzi, A., Dalampakis, P., Falalakis, G., 2021. Detecting geothermal anomalies using Landsat 8 thermal infrared remotely sensed data. *Int. J. Appl. Earth Obs. Geoinf.* 96. https://doi.org/10.1016/j.jag.2020.102283

Ghosal, D., Singh, S.C., Chauhan, A.P.S., Hananto, N.D., 2012. New insights on the offshore extension of the Great Sumatran fault, NW Sumatra, from marine geophysical studies. *Geochemistry, Geophys. Geosystems.* https://doi.org/10.1029/2012GC004122

Hochstein, M.P., Sudarman, S., 2008. History of geothermal exploration in Indonesia from 1970 to 2000. *Geothermics* 37, 220–266. https://doi.org/10.1016/j.geothermics.2008.01.001

Idroes, R., Yusuf, M., Saiful, S., Alatas, M., Subhan, S., Lala, A., Muslem, M., Suhendra, R., Idroes, G.M., Marwan, M., Mahlia, T.M.I., 2019. Geochemistry Exploration and Geothermometry Application in the North Zone of Seulawah Agam, Aceh Besar District, Indonesia. *Energies* 12, 4442. https://doi.org/10.3390/en12234442

Ismail, N., Nadra, U., Yanis, M., 2021. Understanding Volcano Activity Using 2D Simulation Models of MT Data. Proc. - 2nd SEA-STEM Int. Conf. SEA-STEM 2021 129–132. https://doi.org/10.1109/SEA-STEM53614.2021.9668175

Kandari, M., Yulianto, G., Saptadi, S., 2020. Analysis of risk factors nonproductive time on geothermal drilling in Indonesia. *AIP Conf. Proc.* 2217, 030113. https://doi.org/10.1063/5.0000918

Lashin, A., Al Arifi, N., 2014. Geothermal energy potential of southwestern of Saudi Arabia exploration and possible power generation: A case study at Al Khouba area - Jizan. *Renew. Sustain. Energy Rev.* https://doi.org/10.1016/j.rser.2013.10.037

Mansoer, W.R., Idral, A., 2015. Geothermal Resources Development in Indonesia: A History, World Geothermal Congress 2015.

Marwan, Asrillah, Yanis, M., Furumoto, Y., 2019a. Lithological identification of devastated area by Pidie Jaya earthquake through poisson's ratio analysis. *Int. J. GEOMATE* 17, 210–216. https://doi.org/10.21660/2019.63.77489

Marwan, Idroes, R., Yanis, M., Idroes, G.M., Syahriza, 2021. A Low-Cost UAV Based Application For Identify and Mapping a Geothermal Feature in Ie Jue Manifestation, Seulawah Volcano, Indonesia. *Int. J. GEOMATE* 20, 135–142. https://doi.org/10.21660/2021.80.j2044

Marwan, M., Yanis, M., Nugraha, G.S., Zainal, M., Arahman, N., Idroes, R., Dharma, D.B., Saputra, D., Gunawan, P., 2021. Mapping of Fault and Hydrothermal System beneath the Seulawah Volcano Inferred from a Magnetotellurics Structure. *Energies* 14, 6091. https://doi.org/10.3390/en14196091

Marwan, Yanis, M., Idroes, R., Ismail, N., 2019b. 2D inversion and static shift of MT and TEM data for imaging the geothermal resources of Seulawah Agam Volcano, Indonesia. *Int. J. GEOMATE* 17. https://doi.org/10.21660/2019.62.11724

Marwan, Yanis, M., Muzakir, Nugraha, G.S., 2020. Application of QR codes as a new communication technology and interactive tourist guide in Jaboi, Sabang, in: *IOP Conference Series: Materials Science and Engineering*. Institute of Physics Publishing. https://doi.org/10.1088/1757-899X/796/1/012025

Marwan, Yanis, M., Zahratunnisa, Idroes, R., Nugraha, G., Dharma, D.B., Susilo, A., Saputra, D., Suriadi, Paembonan, A.Y., 2022. Geothermal Reservoir Depth of Seulawah Agam Volcano Estimated From 1D Magnetotelluric. *J. Appl. Eng. Sci.* 1–11. https://doi.org/10.5937/JAES0-36077

Mia, M.B., Bromley, C.J., Fujimitsu, Y., 2013. Monitoring Heat Losses Using Landsat ETM + Thermal Infrared Data: A Case Study in Unzen Geothermal Field, Kyushu, Japan. *Pure Appl. Geophys.* https://doi.org/10.1007/s00024-013-0662-1

Mia, M.B., Fujimitsu, Y., Nishijima, J., 2019. Exploration of hydrothermal alteration and monitoring of thermal activity using multi-source satellite images: A case study of the recently active Kirishima volcano complex on Kyushu Island, Japan. *Geothermics.* https://doi.org/10.1016/j.geothermics.2019.01.006

Mia, M.B., Fujimitsu, Y., Nishijima, J., 2017. Thermal Activity Monitoring of an Active Volcano Using Landsat 8/OLI-TIRS Sensor Images: A Case Study at the Aso Volcanic Area in Southwest Japan. *Geosci.* 7. https://doi.org/10.3390/geosciences7040118

Mia, M.B., Nishijima, J., Fujimitsu, Y., 2014. Exploration and monitoring geothermal activity using Landsat ETM+images. A case study at Aso volcanic area in Japan. *J. Volcanol. Geotherm. Res.* https://doi.org/10.1016/j.jvolgeores.2014.02.008

Mohan, K., Chaudhary, P., Kumar, G.P., Kothyari, G.C., Choudhary, V., Nagar, M., Patel, P., Gandhi, D., Kushwaha, D., Rastogi, B.K., 2018. Magnetotelluric Investigations in Tuwa-Godhra Region, Gujarat (India). *Pure Appl. Geophys.* 175, 3569–3589. https://doi.org/10.1007/s00024-018-1883-0

Morifuji, Y., Fujimitsu, Y., Nishijima, J., Mia, M.B., Onizuka, S., 2021. Analysis of Heat Discharge Rate in Geothermal Areas Using Remote Sensing Techniques: Case Study of Unzen Geothermal Area, Japan; Papandayan and Tangkuban Perahu Geothermal Area, Indonesia. *Pure Appl. Geophys.* 178, 2241–2256. https://doi.org/10.1007/s00024-021-02743-w

Mosher, D.C., Austin, J.A., Fisher, D., Gulick, S.P.S., 2008. Deformation of the northern Sumatra accretionary prism from high-resolution seismic reflection profiles and ROV observations. *Mar. Geol.* https://doi.org/10.1016/j.margeo.2008.03.014

Muksin, U., Irwandi, Rusydy, I., Muzli, Erbas, K., Marwan, Asrillah, Muzakir, Ismail, N., 2018. Investigation of Aceh Segment and Seulimeum Fault by using seismological data; A preliminary result. *J. Phys. Conf. Ser.* 1011, 012031. https://doi.org/10.1088/1742-6596/1011/1/012031

Muñoz, G., 2014. Exploring for Geothermal Resources with Electromagnetic Methods. Surv. *Geophys.* https://doi.org/10.1007/s10712-013-9236-0

Mwaniki, M.W., Moeller, M.S., Schellmann, G., 2015. A comparison of Landsat 8 (OLI) and Landsat 7 (ETM+) in mapping geology and visualising lineaments: A case study of central region Kenya. Int. Arch. Photogramm. *Remote Sens. Spat. Inf. Sci.*

Natawidjaja, D.H., Triyoso, W., 2007. The Sumatran fault zone—From source to hazard. *J. Earthq. Tsunami* 1, 21–47.

Qin, Q., Zhang, N., Nan, P., Chai, L., 2011. Geothermal area detection using Landsat ETM+ thermal infrared data and its mechanistic analysis-A case study in Tengchong, China. *Int. J. Appl. Earth Obs. Geoinf.* https://doi.org/10.1016/j.jag.2011.02.005

Ramírez-González, L.M., Aufaristama, M., Jónsdóttir, I., Höskuldsson, Á., þórðarson, þorvaldur, Proietti, N.M., Kraft, G., McQuilkin, J., 2019. Remote sensing of surface Hydrothermal Alteration, identification of Minerals and Thermal anomalies at Sveifluháls-Krýsuvík high-temperature Geothermal field, SW Iceland. *IOP Conf. Ser. Earth Environ. Sci.* 254, 012005. https://doi.org/10.1088/1755-1315/254/1/012005

Rizal, M., Ismail, N., Yanis, M., Muzakir, Surbakti, M.S., 2019. The 2D resistivity modelling on north sumatran fault structure by using magnetotelluric data. *IOP Conf. Ser. Earth Environ. Sci.* 364, 012036. https://doi.org/10.1088/1755-1315/364/1/012036

Romaguera, M., Vaughan, R.G., Ettema, J., Izquierdo-Verdiguier, E., Hecker, C.A., van der Meer, F.D., 2018. Detecting geothermal anomalies and evaluating LST geothermal component by combining thermal remote sensing time series and land surface model data. *Remote Sens. Environ.* 204, 534–552. https://doi.org/10.1016/j.rse.2017.10.003

Sekertekin, A., Arslan, N., 2019. Monitoring thermal anomaly and radiative heat flux using thermal infrared satellite imagery – A case study at Tuzla geothermal region. *Geothermics* 78, 243–254. https://doi.org/10.1016/j.geothermics.2018.12.014

Sieh, K., Natawidjaja, D., 2000. Neotectonics of the Sumatran fault, Indonesia. *J. Geophys. Res. Solid Earth* 105, 28295–28326. https://doi.org/10.1029/2000JB900120

Silvestri, M., Marotta, E., Buongiorno, M.F., Avvisati, G., Belviso, P., Sessa, E.B., Caputo, T., Longo, V., Leo, V. De, Teggi, S., 2020a. Monitoring of surface temperature on parco delle biancane (Italian geothermal area) using optical satellite data, UAV and field campaigns. *Remote Sens.* 12. https://doi.org/10.3390/rs12122018

Silvestri, M., Romaniello, V., Hook, S., Musacchio, M., Teggi, S., Buongiorno, M.F., 2020b. First comparisons of surface temperature estimations between ECOSTRESS, ASTER and landsat 8 over Italian volcanic and geothermal areas. *Remote Sens.* 12. https://doi.org/10.3390/RS12010184

Sobrino, J.A., Jiménez-Muñoz, J.C., Sòria, G., Romaguera, M., Guanter, L., Moreno, J., Plaza, A., Martínez, P., 2008. Land surface emissivity retrieval from different VNIR and TIR sensors, in: IEEE Transactions on Geoscience and Remote Sensing. pp. 316–327. https://doi.org/10.1109/TGRS.2007.904834

Suryadarma, Dwikorianto, T., Zuhro, A.A., Yani, A., 2010. Sustainable development of the Kamojang geothermal field. *Geothermics* 39, 391–399. https://doi.org/10.1016/J.GEOTHERMICS.2010.09.006

USGS, 2015. Landsat 8 (L8) Data Users Handbook, Earth Resources Observation and Science (EROS) Center.

Van der Meer, F., Hecker, C., van Ruitenbeek, F., van der Werff, H., de Wijkerslooth, C., Wechsler, C., 2014. Geologic remote sensing for geothermal exploration: A review. *Int. J. Appl. Earth Obs. Geoinf.* https://doi.org/10.1016/j.jag.2014.05.007

Watson, F.G.R., Lockwood, R.E., Newman, W.B., Anderson, T.N., Garrott, R.A., 2008. Development and comparison of Landsat radiometric and snowpack model inversion techniques for estimating geothermal heat flux. *Remote Sens. Environ.* 112, 471–481. https://doi.org/10.1016/J.RSE.2007.05.010

Weng, Q., Lu, D., Schubring, J., 2004. Estimation of land surface temperature-vegetation abundance relationship for urban heat island studies. *Remote Sens. Environ.* 89, 467–483. https://doi.org/10.1016/j.rse.2003.11.005

Yanis, M., Abdullah, F., Zaini, N., Ismail, N., 2021a. The northernmost part of the Great Sumatran Fault map and images derived from gravity anomaly. *Acta Geophys.* 69, 795–807. https://doi.org/10.1007/s11600-021-00567-9

Yanis, M., Faisal, A., Yenny, A., Muzakir, Z., Abubakar, M., Nazli, I., 2020a. Continuity of Great Sumatran Fault in the Marine Area revealed by 3D Inversion of Gravity Data. *J. Teknol.* 83, 145–155. https://doi.org/10.11113/jurnalteknologi.v83.14824

Yanis, M., Ismail, N., Abdullah, F., 2022a. Shallow Structure Fault and Fracture Mapping in Jaboi Volcano, Indonesia, Using VLF–EM and Electrical Resistivity Methods. *Nat. Resour. Res.* 31, 335–352. https://doi.org/10.1007/s11053-021-09966-7

Yanis, M., Marwan, 2019. The potential use of satellite gravity data for oil prospecting in Tanimbar Basin, Eastern Indonesia. *IOP Conf. Ser. Earth Environ. Sci.* 364, 012032. https://doi.org/10.1088/1755-1315/364/1/012032

Yanis, M., Marwan, Idroes, R., Zaini, N., Paembonan, A.Y., Ananda, R., Ghani, A.A., 2022b. A pilot survey for mapping the fault structure around the Geuredong volcano by using high-resolution global gravity. *Acta Geophys.* 2022 1–19. https://doi.org/10.1007/S11600-022-00860-1

Yanis, M., Marwan, M., Paembonan, A.Y., Yudhyantoro, Y., Rusydy, I., Idris, S., Asrillah, A., 2021b. Geophysical and Geotechnical Approaches in Developing Subsurface Model for Gas Power Plant Foundation. *Indian Geotech. J.* https://doi.org/10.1007/s40098-021-00559-y

Yanis, M., Novari, I., Zaini, N., Marwan, Pembonan, A.Y., Nizamuddin, 2020b. OLI and TIRS Sensor Platforms for Detection the Geothermal Prospecting in Peut Sagoe Volcano, Aceh Province, Indonesia, in: 2020 International Conference on Electrical Engineering and Informatics (ICELTICs). IEEE, pp. 1–6. https://doi.org/10.1109/ICELTICs50595.2020.9315378

Zaini, N., Yanis, M., Abdullah, F., Van Der Meer, F., Aufaristama, M., 2022. Exploring the geothermal potential of Peut Sagoe volcano using Landsat 8 OLI/TIRS images. *Geothermics* 105, 102499. https://doi.org/10.1016/j.geothermics.2022.102499

Zaini, N., Yanis, M., Marwan, Isa, M., van der Meer, F., 2021. Assessing of land surface temperature at the Seulawah Agam volcano area using the landsat series imagery, in: *Journal of Physics: Conference Series*. https://doi.org/10.1088/1742-6596/1825/1/012021